



Cite this: DOI: 10.1039/c8nr01070f

## Ni-core CuO-shell fibers produced by electrospinning and electroplating as efficient photocathode materials for solar water splitting†

Hong-Seok Jo,<sup>‡a</sup> Min-Woo Kim,<sup>‡a</sup> Bhavana Joshi,<sup>a</sup> Edmund Samuel,<sup>a</sup> Hyun Yoon,<sup>b</sup> Mark T. Swihart<sup>Ⓜc</sup> and Sam S. Yoon<sup>Ⓜ\*a</sup>

Charge recombination in CuO photocathodes inhibits efficient electron flow and limits the photoelectrochemical performance of these cathodes for solar water splitting. To circumvent this shortcoming, we introduce highly conductive Ni/CuO core-shell structured fibers. The photocurrent density (PCD) achieved with these core-shell fibers exceeded that of fibers without a Ni core by a factor of 2.6. The PCD enhancement arises from increased acceptor concentration and electron-hole recombination time, as measured by electrochemical impedance spectroscopy. These core-shell nanofibers were fabricated via electrospinning and electroplating. First, a polyacrylonitrile fiber was electrospun and then seeded with metal via sputtering. Second, electroplating was used to encase and metalize the fiber with Ni and Cu. Finally, the outermost Cu shell was oxidized to CuO, which is an effective photocathode for solar water splitting. The Ni-CuO, core-shell layers were characterized by scanning electron microscopy, elemental mapping, X-ray diffraction, and X-ray photoelectron spectroscopy. The core Ni content and number of core-shell fibers per area were optimized through parametric studies.

Received 5th February 2018,

Accepted 6th May 2018

DOI: 10.1039/c8nr01070f

rsc.li/nanoscale

## 1. Introduction

H<sub>2</sub> generation from solar-driven water splitting by photoelectrochemical (PEC) processing has shown immense potential as a source of clean energy.<sup>1,2</sup> As a fuel, H<sub>2</sub> exhibits a specific energy density about three times that of gasoline.<sup>3</sup> In general, PEC performance is determined by the electrode characteristics, such as electrical conductivity, bandgap, and recombination rate. The commercialization of PEC-based hydrogen production is hindered by the low efficiency, chemical instability, and high cost of PEC cells.<sup>4</sup> Preparation of photoelectrodes from earth-abundant elements to lower the cost of such cells is therefore of great interest. Multilayer heterojunction structures with maximized light absorbance would improve the solar efficiency of a PEC cell. The chemical

stability of cells can be improved by adding thin protective layers to the electrode-electrolyte interface.<sup>5-7</sup>

In general, PEC devices use n-type semiconductors as photoanodes at which oxygen is produced, and p-type semiconductors as photocathodes at which hydrogen is produced. NiO, CuO, and Co<sub>3</sub>O<sub>4</sub> have been used as photocathode materials.<sup>8,9</sup> Nanostructured electrodes often provide improved PEC performance by increasing the number of reactive sites at the electrode-electrolyte interface.<sup>8,10</sup> CuO has a bandgap of 1.3–1.8 eV, and thus can absorb the majority of the visible light spectrum. In addition, CuO is naturally abundant and nontoxic; thus, it shows promise as a commercial photocathode candidate. However, the low conductivity of CuO induces a high electron-hole recombination rate after photoexcitation. This rapid charge recombination causes rapid electron depletion at the electrode-electrolyte interface, leading to poor PEC performance. In general, two methods can be used to overcome this rapid electron depletion: doping with metals such as Co, Ni, Fe, and Mn, and the introduction of heterojunction layers.<sup>11-13</sup> Metallic doping enhances electrical conductivity while heterojunction layers facilitate electron trapping, which generally enhances electron-hole separation.

Baturay *et al.*<sup>14</sup> doped CuO with Ni and demonstrated an improved PEC cell with increased electron mobility. Chiang *et al.*<sup>12</sup> introduced eight different doping materials to investigate their effects on the PEC performance of CuO. They concluded

<sup>a</sup>School of Mechanical Engineering, Korea University, Seoul 02841, Republic of Korea. E-mail: skyoon@korea.ac.kr

<sup>b</sup>KIER-UNIST Advanced Center for Energy, Korea Institute of Energy Research (KIER), 50, UNIST-gil, Ulsan 44919, Republic of Korea

<sup>c</sup>Department of Chemical & Biological Engineering, University at Buffalo, The State University of New York, Buffalo, New York 14260-4200, USA

†Electronic supplementary information (ESI) available. See DOI: 10.1039/c8nr01070f

‡These authors have contributed equally.

that Li and Ni were the most suitable for PCD enhancement. Ni addition altered the  $H^+$  binding energy, which rapidly released electrons towards the surface to promote PEC activity. Ha *et al.*<sup>13</sup> used Ni as a dopant for a nanostructured CuO photocathode and demonstrated PCD enhancement. Dubale *et al.*<sup>15</sup> used Ni as a co-catalyst electrodeposited on  $Cu_2O/CuO$  layers.

Herein, we fabricate a Ni fiber encased by a Cu shell, thereby forming a novel Ni–Cu core–shell nanofiber for use as a hybrid photocathode material. The post-annealing process converts the Cu outer shell to semiconducting CuO, allowing the fiber to function as a photoactive material while the inner Ni remains metallic and highly electrically conductive. The network of conductive Ni cores with thin CuO shells provides rapid transport of electrons from the external circuit; thus, the recombination rate is reduced significantly.<sup>16</sup> The fibrous structure of the electrode increases the surface-to-volume ratio, thereby increasing the number of reaction sites and decreasing the transport distance for photogenerated carriers. The one-dimensional nature of the fiber also contributes to the rapid transport of electrons from the external circuit. We investigated the effect of the amount of Ni on the overall PEC performance by controlling the electrospinning time used to fabricate the Ni fiber.

## 2. Experimental section

### 2.1 Materials

The electrospinning solution for fabricating polymer nanofibers was formed by dissolving 8 wt% and 6 wt% polyacrylonitrile (PAN,  $M_w = 150$  kDa, Sigma-Aldrich, USA) in *N,N*-dimethylformamide (DMF, 99.8%, Sigma-Aldrich, USA). The solution of Ni for electroplating was prepared by blending 80 g  $Ni(SO_3NH_2)_2 \cdot 4H_2O$  (Sigma-Aldrich, USA) and 6 g  $H_3BO_3$  (Sigma-Aldrich, USA) in 200 mL deionized (DI) water; the pH was adjusted to 4.5 by adding 1 M NaOH (Sigma-Aldrich, USA). The Cu electroplating solution was prepared by mixing 5 g  $H_2SO_4$  (Matsuo Chemicals, South Korea), 0.5 g HCl (Sigma-Aldrich, USA), 13 g  $CuSO_4$  (Sigma-Aldrich, USA), and 10 g formaldehyde (Sigma-Aldrich, USA) in 100 mL DI water, followed by stirring for 1 h at room temperature.

### 2.2 Preparation of Ni and CuO fibers

The overall process of manufacturing photocathodes from Ni fibers (Ni Fs) and CuO fibers (CuO Fs) is presented in Fig. 1.

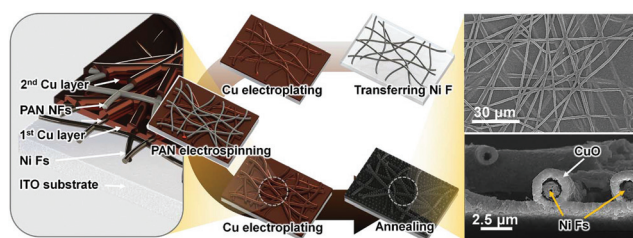


Fig. 1 Schematic of the manufacturing process for Ni fiber and CuO fiber layers.

The fabrication of Ni F proceeded as follows: first, the 8 wt% PAN solution was electrospun for deposition times of  $t_e = 5, 10, 20,$  and  $30$  s, onto a square Cu frame measuring  $2 \times 1$  cm<sup>2</sup>. The precursor was supplied at  $200 \mu\text{L h}^{-1}$  and 5.5 kV using a needle (25 gauge, EFD), a syringe pump (Legato 100, KD Scientific), and a DC power supply (EL20P2, Glassman high voltage). Second, Pt particles were deposited by sputtering (Vacuum Device Inc., MSP-1S) on the nanofiber surface for Ni electroplating. Third, the Pt-decorated nanofibers were electroplated with Ni at an applied voltage of 6 V and electroplating time  $t_{Ni} = 10$  s. Finally, the Ni fibers were transferred to a  $2 \times 1$  cm<sup>2</sup> In-doped Sn oxide (ITO) coated glass substrate and dried with  $N_2$  for a few seconds.

For CuO photocathode preparation, Cu was electroplated onto the ITO substrate bearing the Ni Fs at an applied voltage of 1 V for 10 s. The electroplated Ni/Cu Fs on ITO were rinsed with water and dried with  $N_2$  gas for a few seconds. Next, one more layer of PAN (6 wt%) nanofibers was electrospun for 60 s at  $130 \mu\text{L h}^{-1}$  and 5 kV over the Ni/Cu Fs. Then the PAN nanofibers were seeded with Pt nanoparticles and electroplated again with Cu for 15 s. This second cycle of electrospinning and electroplating was required to produce a sufficiently thick CuO layer for optimal absorbance of light while also providing an overall average CuO concentration gradient from the electrode–electrolyte interface (pure CuO) to the fiber mat–ITO interface. This overall composition gradient can facilitate charge separation. The Ni/Cu@PAN/Cu Fs on ITO were rinsed with water and dried. Finally, the samples were heated at a rate of  $5 \text{ }^\circ\text{C min}^{-1}$  to  $500 \text{ }^\circ\text{C}$  and annealed at  $500 \text{ }^\circ\text{C}$  in air for 1 h, yielding Ni/CuO fibers. The CuO formed a layered structure over the ITO as well as the core–shell Ni–CuO structures after annealing. Hence, the Ni core is henceforth described as the under-layer.

### 2.3 Photoelectrochemical and electrochemical impedance spectroscopy (EIS) measurements

The photoelectrochemical characteristics of the Ni/CuO Fs were measured by a three-electrode cell. The Ni/CuO Fs, an Ag/AgCl electrode, and a Pt wire were used as the working, reference, and counter electrodes, respectively. The electrolyte was a 1 M KOH (pH = 14) solution. The photocathode was illuminated from the front side with artificial sunlight by a Xe arc lamp with an AM 1.5 filter (Newport Oriel Instruments, USA) at an intensity of  $100 \text{ mW cm}^{-2}$ . The distance from the photocathode to the lamp was adjusted to the light intensity of  $100 \text{ mW cm}^{-2}$  using a power meter (1919-R, Newport Oriel Instruments, USA) and an optical sensor (918D-UV-OD3R, Newport Oriel Instruments, USA), and fixed near 10 cm. The photocathode of  $1 \times 1$  cm<sup>2</sup> area was immersed into the electrolyte. All photocurrent data were recorded by a potentiostat (VersaSTAT-3, Princeton Applied Research, USA) at a scan rate of  $10 \text{ mV s}^{-1}$  over the applied voltage range of 0.1 to  $-0.5$  V with Ag/AgCl as the reference electrode. The electrochemical impedance was characterized using the same VersaSTAT-3 setup under light. The frequency range was from 100 kHz to

0.1 Hz and the AC amplitude was 10 mV during the measurements.

## 2.4 Characterization

The morphologies and elemental compositions of the Ni and CuO Fs were analyzed using a scanning electron microscope (SEM, S-5000, Hitachi), a field-emission SEM with energy-dispersive X-ray spectroscopy (FE-SEM/EDX, Quanta 250 FEG, FEI), and a field-emission TEM (Tecnai G2 F30ST, Thermo Fisher Scientific). The sheet resistances of the Ni Fs were measured by a sheet resistance meter (FPP-400, Dasol ENG). The phases and oxidation states of the Ni/CuO Fs after annealing at 500 °C were identified by X-ray diffraction (XRD, SmartLab, Rigaku), X-ray photoelectron spectroscopy (XPS, Theta probe base system or Ulvac PHI/X-tool), and UV-VIS-NIR spectrophotometry (Cary 5000, Agilent Technologies), respectively.

## 3. Results and discussion

### 3.1 Film characterization

Fig. S1† shows top-view SEM images of the Ni Fs on ITO for different electrospinning times  $t_e$ . The diameters ( $D$ ) of the Ni Fs decrease as the  $t_e$  is increased from 5 to 30 s, because the amount of Ni electroplated per unit area decreases as the total surface area of PAN nanofibers increases, at a fixed electroplating time ( $t_{Ni}$ ). At the same time, the electroplating current increases with increasing  $t_e$  (increasing fiber surface area), so that the total amount of nickel electroplated increases with increasing  $t_e$ , even as the amount per fiber decreases. As shown in Table 1, the sheet resistance ( $R_s$ ) decreases from 4.8 to 2.2  $\Omega \text{ sq}^{-1}$  with increasing  $t_e$ . This shows that the effect of the increased number of Ni F junctions, increased number of fibers, and increased total amount of Ni, all of which decrease sheet resistance, is greater than the effect of the decrease in  $D$ , which increases the resistance of each fiber. This three dimensional network of sub-micron Ni Fs with high electrical conductivity promotes fast charge transfer and allows high current densities at low potential.

Fig. 2 shows SEM images of the Ni/CuO Fs for  $t_e = 5, 10, 20,$  and 30 s. Ni Fs are enveloped and buried after the second round of Cu electroplating, as shown in Fig. 2a. However, with increasing  $t_e$  and the resulting increased areal density of Ni Fs, the deposited fibers form multilayer structures. The fraction of Ni Fs encased in CuO is decreased in these multilayer structures. Further, the diameter of the top-layer CuO Fs also

decreased with increased areal density of Ni Fs (see Fig. 2b). When  $t_e = 5$  s for the Ni Fs, the diameter of CuO Fs at the top is approximately 2.3  $\mu\text{m}$ ; this decreases to 2.0, 1.5, and 1.1  $\mu\text{m}$  as  $t_e$  increases to 10, 20, and 30 s, as shown in Fig. 2b. This decreased diameter of top-layer CuO Fs may be attributed to the preferential electroplating of Cu on the highly conductive surfaces of Ni/Cu fibers prepared in the first electroplating time, relative to the lower conductivity of the newly spun PAN nanofibers with Pt-seeding. Fig. 2c shows cross-sectional SEM images of CuO Fs over Ni F (deposited for  $t_e = 5, 10, 20,$  and 30 s). Moreover, Fig. 2d reveals the axial core structure of the Ni/CuO Fs after the first electroplating step, where CuO covering the Ni cores is verified by the elemental mapping of Cu, O, and Ni. Some traces of O observed over the Ni core may arise from annealing at 500 °C.

The cross sectional image of Ni/CuO Fs analysed by transmission electron microscopy, presented in Fig. 3a, confirms the formation of Ni/CuO core-shell fibers. Elemental mapping of the fiber shows a thicker Cu (red) and O (yellow) domain, consistent with formation of CuO as a shell layer. The central region of the fiber shows the presence of Ni (blue), while oxygen is observed only at the interface of Ni/CuO forming a thin layer of NiO. This confirms that the core is metallic Ni, which can support fast electron transport towards CuO in PEC tests. Moreover, the SAED pattern (Fig. 3b) was obtained from three different areas of fibers, marked as A, B and C in Fig. 3a. The characteristic rings of Ni corresponding to (010), (011), (110) and (114) planes are observed in the core region (A Part) where no NiO related diffraction rings are observed, further confirming the presence of a metallic Ni core. The interface area labelled B shows diffraction rings of NiO and CuO indexed as (122), (024) and ( $\bar{1}11$ ), (111), (202), (220) planes respectively. The shell region labelled C shows (110) (111), (112), (202), (004) (130) planes attributed to CuO. The reflections of Ni, NiO and CuO in SAED are in agreement with JCPDS cards 41-1027, 44-1159 and 72-0629 respectively.

The overall crystalline phases of CuO and Ni were determined from the XRD patterns of the Ni/CuO Fs, shown in Fig. 4a. Here, Ni was electroplated on fibers electrospun for 20 s. Then, after two layers of Cu electroplating, the sample was annealed at 500 °C. The diffraction peaks of Ni are observed at  $2\theta$  values of 44.4 and 51.8°. Because Ni is located at the core and constitutes a smaller fraction of the overall sample compared to CuO, its diffraction peak intensity is lower than that of CuO. In addition to Ni, the broad hump around 44° could indi-

**Table 1** Parameters of Ni Fiber and Ni–CuO F composites

Ni fiber				Ni–CuO F composites			
Parameter	$t_e$ [s]	$\Omega \text{ sq}^{-1}$	$D$ [ $\mu\text{m}$ ]	$R_{ct1}$ [ $\Omega$ ]	$R_{ct2}$ [ $\Omega$ ]	$C_2$ [ $10^{-7}$ F]	$\tau_n$ [ $10^{-4}$ s]
1	5	4.8	1.53	325	647	8.83	5.72
2	10	3.4	1.25	312	932	9.02	8.41
3	20	2.9	1.05	287	1179	10.4	12.2
4	30	2.2	0.95	267	653	12.1	7.88

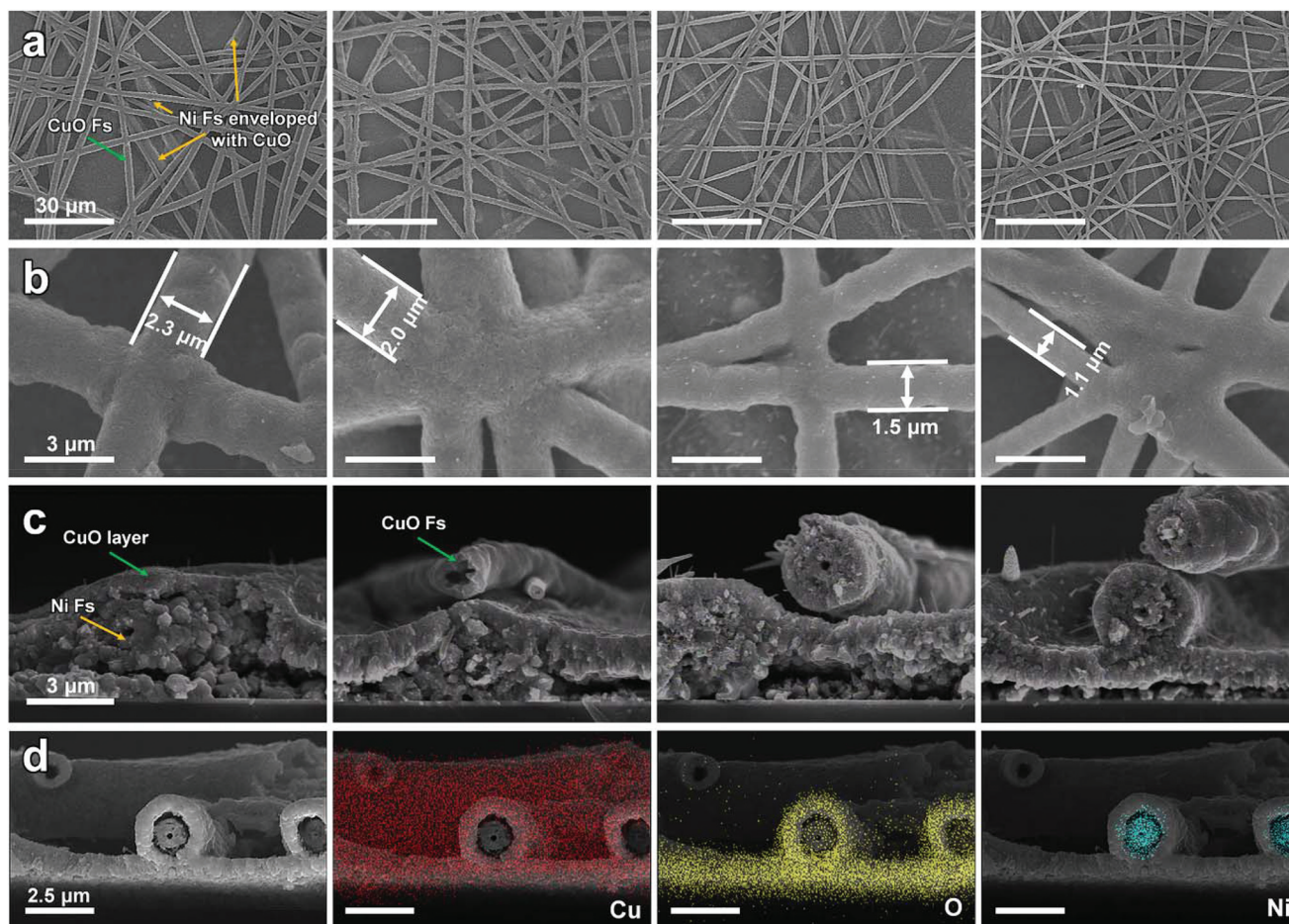


Fig. 2 Top-view SEM images of Ni–CuO ( $t_e = 5, 10, 20$  and  $30$  s) fibers, (a) low-magnification and (b) high-magnification. (c) Cross-section view of Ni–CuO ( $t_e = 5, 10, 20$  and  $30$  s) fibers and (d) elemental mapping of Ni–CuO core-shell fibers with  $t_e = 20$  s.

cate some NiO formation. The dominant CuO peaks are observed at  $2\theta$  values of  $32.5, 35.6, 38.7, 48.9, 53.4, 58.2, 61.6, 65.8, 66.5, 67.9, 72.5,$  and  $75.2^\circ$ , corresponding to the (110), (−111), (111), (−202), (020), (202), (−113), (022), (−311), (113), (311), and (−222) planes, respectively; these are consistent with

the reference JCPDS file 72-0629. The annealing temperature used for the oxidation of Cu,  $500^\circ\text{C}$ , was high enough to form CuO; thus, no impurity phase of  $\text{Cu}_2\text{O}$  is observed.<sup>17–19</sup>

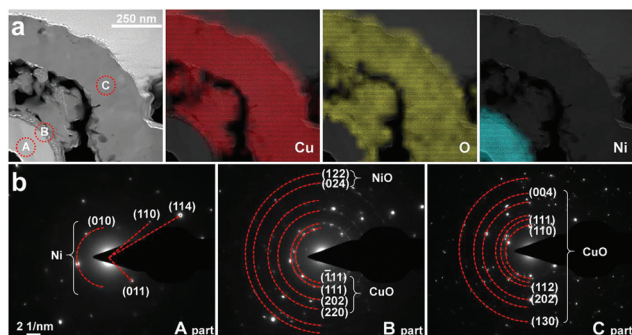


Fig. 3 (a) Cross-sectional TEM image and elemental maps of Cu, O and Ni for Ni–CuO  $t_e = 20$  s photoelectrode. (b) SAED patterns of three parts marked in (a) confirm the metallic Ni core at position A, the presence of ultra-thin NiO at the interface of Ni/CuO (position B) and the CuO layer coated as an outer shell at position C.

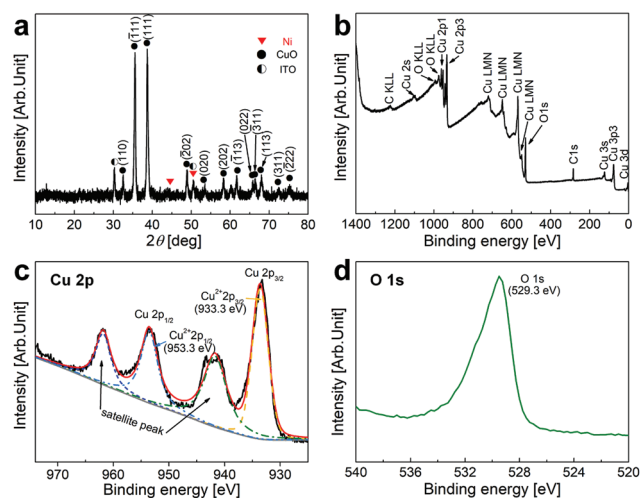


Fig. 4 (a) XRD pattern of Ni/CuO Fs. XPS spectra of Ni/CuO Fs: (b) survey spectrum and high-resolution spectra of (c) Cu 2p and (d) O 1s.

Oxidation at 500 °C for sufficient time leads to complete conversion of Cu<sub>2</sub>O to CuO by the overall reaction:<sup>20</sup>



Single phase CuO has lower band gap energy (~1.76 eV) than Cu<sub>2</sub>O which allows it to contribute to photocatalytic water-splitting with low-energy (longer wavelength) photons.<sup>21</sup>

The Ni/CuO film was investigated by XPS to analyze the composition, oxidation states, and electronic structure. The XPS survey spectrum of the Ni/CuO Fs in Fig. 4b shows peaks at binding energies of 529 and 933 eV, corresponding to the O 1s and Cu 2p orbitals, respectively. Ni peaks are not detected, because Ni is enveloped by a thick CuO layer and the XPS scan depth is only ~10 nm. The C 1s peak observed at 285 eV is due to unavoidable environmental contamination during the preparation of the sample for XPS analysis. As shown in Fig. 4c, the Cu 2p core spectrum shows peaks at 933.5 and 953.3 eV, attributed to Cu 2p<sub>3/2</sub> and Cu 2p<sub>1/2</sub>, respectively. The spin-orbit splitting between Cu 2p<sub>3/2</sub> and Cu 2p<sub>1/2</sub> is 19.8 eV, as expected for CuO.<sup>22,23</sup> The satellite peaks observed at 942.3 and 961.8 eV are characteristic of the Cu<sup>2+</sup> state, verifying CuO formation in a manner consistent with previous reports.<sup>24,25</sup> The O 1s peak at 529.3 eV (Fig. 4d) is at the expected position for CuO.<sup>26,27</sup> The O 1s core peak at 529.3 eV is assigned to lattice oxygen and is characteristic of O<sup>2-</sup> interacting with Cu<sup>2+</sup> to form Cu–O.<sup>28</sup> Thus, XPS suggests that a single oxygen species is present in hybrid Ni–CuO fibers.

Fig. S2a† shows the diffuse reflectance (DR) spectra for wavelengths ( $\lambda$ ) from 175 to 800 nm. The peaks of DR were observed at 240 and 625 nm. The optical band gap can be obtained using the Tauc method:<sup>29</sup>

$$(\alpha h\nu)^{1/n} = A(h\nu - E_g) \quad (2)$$

where  $h$ ,  $\nu$ ,  $A$ , and  $E_g$  are Planck's constant, the frequency of the photon, a proportionality constant, and the band gap, respectively. The absorption coefficient,  $\alpha$ , was estimated as  $\alpha = F(R) = (1 - R)^2/2R$ ,<sup>30</sup> where  $R$  is the diffuse reflectance. Fitting was performed using  $n = 1/2$ , which is characteristic of a direct band-to-band transition.<sup>31</sup> In the Tauc plot, according to eqn (2), the x-intercept of the plot of  $(\alpha h\nu)^{1/n}$  vs.  $h\nu$  gives the photon energy corresponding to the band gap,  $E_g$ .

In the  $h\nu$  range of 2.5 to 5.0 eV, corresponding to 250–620 nm, in which the  $E_g$  of NiO can be identified, the peak was 625 nm in Fig. S2a† and  $E_g$  of NiO can be observed at 3.8 eV in the present study (Fig. S2b†). The  $E_g$  value of CuO was also found to be 1.67 eV as shown in Fig. S2c.†

### 3.2 Photoelectrochemical properties

The outcome of the kinetic competition between electron-hole recombination (within the photocathode) and water splitting depends upon various parameters such as Ni F diameter, sheet resistance, acceptor concentration, carrier recombination time within CuO, and charge transfer resistances at the Ni F–CuO interface and the CuO–electrolyte interface. Fig. 5a

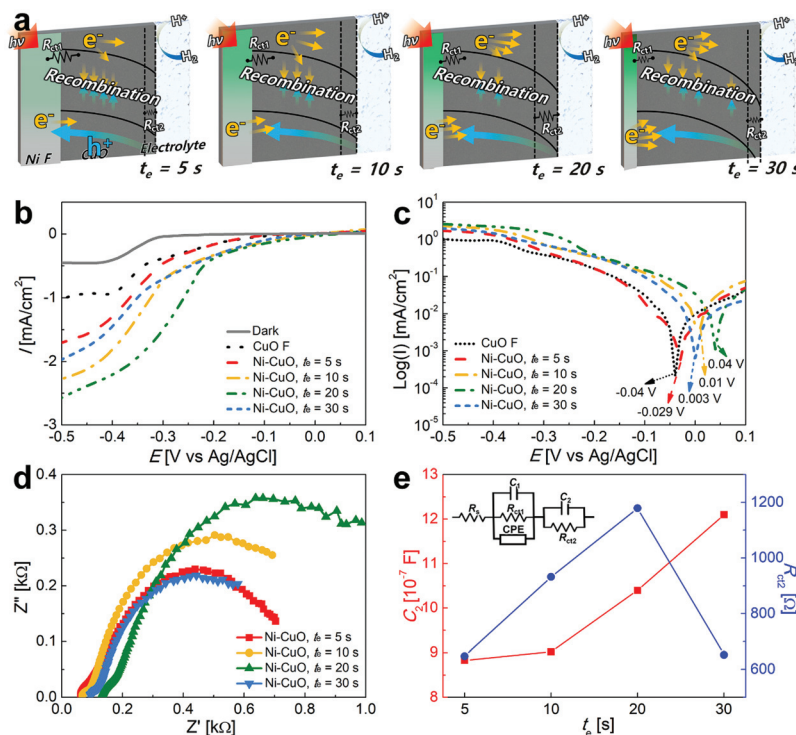


**Fig. 5** (a) Kinetic mechanism of photocathodes. (b) Effect of the areal density of Ni Fs (increased with increasing  $t_e$ ) on the PCD and (c) current-voltage plot, presented as  $\log(j)$  versus  $V$ . (d) Nyquist plots of EIS data measured under 1 sun illumination. (e) The charge transfer resistance ( $R_{ct2}$ ) and capacitance ( $C_2$ ) for varied electrospinning times. Inset schematic: the equivalent electrical circuit used for fitting the EIS data.

depicts the influence of these parameters. Increasing the electrospinning time decreases Ni F diameter (see SEM images in Fig. 2), which in turn increases the current density within the Ni F, as indicated by the arrows in Fig. 5a. Electrons from the Ni F are transferred to the CuO layer, as the photoexcited electrons generated by absorption of incident photons are transported to the CuO–electrolyte interface, where a surface charge region is developed.

Because of the reduced Ni F diameter, the charge transfer resistance ( $R_{ct1}$ ) at the Ni F–CuO interface is reduced; the thickness of the surface charge region at the CuO–electrolyte interface is increased; the charge transfer resistance ( $R_{ct2}$ ) is increased; the recombination time is also increased. We have estimated these charge transfer resistances and recombination times from results of electrochemical impedance spectroscopy, as presented in Table 1. It is important to note that, in the fourth case, even though more electrons from the Ni Fs reach the CuO layer, the lower acceptor concentration of CuO resulted in more recombination, ultimately reducing the surface charge region, as reflected in the increased  $R_{ct2}$ . Additionally, the total CuO layer thickness was found to be 5.04, 5.12, 5.62 and 5.91  $\mu\text{m}$  for  $t_e = 5, 10, 20$  and  $30$  s, respectively.

Fig. 5b demonstrates the significant effect of Ni Fs as an under-layer for CuO, forming a novel morphology with improved PCD. The synergistic effects of Ni F and CuO are observed for all Ni/CuO F specimens. Moreover, the Ni–CuO F with the electrospinning time of 20 s demonstrates the highest PCD among all tested samples, reaching 2.6  $\text{mA cm}^{-2}$  at  $-0.5$  V. It shows a 2.6-fold enhancement in PCD compared to CuO-only Fs (1  $\text{mA cm}^{-2}$  at  $-0.5$  V). The improved photoelectrochemical performance suggests that the structural modification using Ni Fs as an under-layer for CuO improves water-splitting performance through improved efficiency of charge transfer. The PCD values for Ni–CuO Fs with electrospinning times of 5, 10, and 30 s are 1.7, 2.3, and 1.9  $\text{mA cm}^{-2}$  at  $-0.5$  V, respectively. Thus, increasing  $t_e$  from 0 to 20 s for Ni Fs is shown to increase the PCD. However, for Ni–CuO Fs electrospun for 30 s the PCD decreases to  $\sim 2$   $\text{mA cm}^{-2}$ . This could be attributed to the higher areal density of Ni Fs, which increases electron concentration at the Ni F/CuO F interface as evident by lower  $R_{ct1}$ . Further, more electron transfer from Ni F ( $t_e = 30$  s) reduced the driving force for electron–hole separation. Thus, the surface charge layer (see Fig. 5a) and overall  $N_A$  (acceptor concentration) of the CuO layer are reduced. During biasing condition and under illumination the electron–hole recombination becomes fast leading to lower availability of electrons at the interface and reduced photocurrent. The rise in electron–hole recombination during PEC measurements is well supported by reduced recombination time ( $\tau_n$ ) and  $R_{ct2}$  as presented in Table 1. Furthermore, the improved PCD is consistent with the onset potential revealed by the current–voltage ( $I$ – $V$ ) characteristics as plotted on a semi-logarithmic scale. The onset potential is enhanced by 0.1 V for the Ni–CuO Fs electrospun for 20 s relative to that of CuO-only Fs, as indicated in Fig. 5c. The reduced onset potential observed in

Fig. 5c is attributed to the fast electron transport through the Ni Fs, corresponding to the lower sheet resistance of Ni (see Table 1).

To examine the influence of the Ni F thickness as well as that of the CuO over-layer on the photocathode performance, electrochemical impedance spectra (EIS) studies, were performed under 1 sun illumination ( $100 \text{ mW cm}^{-2}$ ). The impedance ( $Z$ ) shows time and frequency dependence with respect to the alternating potential ( $E_t$ ) and current ( $I_t$ ) as follows:

$$Z(\omega) = \frac{E_0 e^{j\omega t}}{I_0 e^{j(\omega t - \theta)}} = Z_0 (\cos \theta - j \sin \theta) \quad (3)$$

The impedance  $Z(\omega)$  can be separated to real and imaginary impedance. The real and imaginary impedance can be represented as follows:

$$Z' = Z_{\text{real}} = Z_0 \cos \theta \quad (4)$$

$$Z'' = Z_{\text{imag}} = Z_0 \sin \theta \quad (5)$$

Although the impedance varies with the frequency (100 kHz–0.1 Hz), one can plot real and imaginary impedances against one another. This plot is conventionally known as a Nyquist plot and it provides valuable insight into charge transfer and electrolyte ion diffusion during the electrochemical process. The impedance increases with decrease in frequency, thus lower impedance corresponds to higher frequency and *vice versa*.

Fig. 5d shows Nyquist plots for the Ni–CuO Fs photocathodes in the frequency range from 100 kHz to 0.1 Hz. The EIS data were fitted using the Randles equivalent circuit, shown as the inset in Fig. 5e. The first impedance value (at 100 kHz) corresponds to the series resistance ( $R_s$ ) associated with the interface between the ITO substrate and the deposited photocathode materials. The smaller high-frequency semicircle is attributed to the developed Helmholtz resonance at the ITO/Ni F interface, which generates charge-transfer resistance ( $R_{ct1}$ ) and capacitance ( $C_1$ ) in the Ni Fs. The derived values of the resistance and capacitance for the Randle equivalent circuit are provided in Table 1. The charge transfer resistance is observed to decrease with decreasing Ni F diameter, as shown in Table 1. However, the second semicircle formed by real and imaginary impedance that corresponds to middle–low frequencies reflects an additional resistance  $R_{ct2}$ . The second charge transfer resistance ( $R_{ct2}$ ) also shows proportional correlation to the Ni F diameter, except for the Ni–CuO F electrospun for 30 s. The sudden drop in impedance is attributed to the lower sheet resistance and smaller diameter, which may accelerate electron transport from the Ni F and thereby decrease the overall resistance of the photocathode.  $C_2$  indicates the capacitance due to charge accumulation from the electron–hole separation in the CuO layers. The capacitance  $C_2$  and resistance  $R_{ct2}$  at the surface of the photocathode are presented in Fig. 5e.<sup>32</sup> Furthermore, the recombination lifetimes ( $\tau_n$ )

presented in Table 1 are calculated by using Eqn (6) as follows:<sup>33,34</sup>

$$\tau_n = R_{ct2} \times C_2 \quad (6)$$

The values for  $C_2$  and  $R_{ct2}$  were obtained by fitting the Nyquist data measured from EIS to estimate the recombination time for all photocathodes. The recombination time ( $\tau_n$ ) for Ni Fs at  $t_e = 20$  s, is the highest at  $12.2 \times 10^{-4}$  s. In this case, a thicker surface charge region is formed as shown in Fig. 5a. The thicker surface charge region is formed because of reduced recombination in the bulk region and it boosts the efficiency of electron transport for reaction at the CuO–electrolyte interface to yield superior PCD in comparison to that of other samples, as demonstrated in Fig. 5b. These results are consistent with the Mott–Schottky measurements discussed later, from which the acceptor concentrations are calculated as being higher for the  $t_e = 20$  s case compared to other samples. Thus, electron–hole separation after photoexcitation, rather than recombination, is the dominant pathway, which provides more electrons at the interface. This resulted in higher surface charge and consequently larger charge-transfer resistance ( $R_{ct2} = 1179 \Omega$ ) near the surface of CuO.<sup>35</sup>

### 3.3 Effect of the number of Ni fibers on the acceptor concentration

To determine the concentration of acceptors in the Ni/CuO F photocathodes, the Mott–Schottky method was employed using measurements performed at a frequency of 1000 Hz with an applied reverse bias of 0.3 to  $-0.05$  V for the p-type semiconductor. In addition, the square reciprocal of the charge capacitances ( $1/C^2$ ) was measured by the Mott–Schottky method; this is given by eqn (7).<sup>35,36</sup>

$$\frac{1}{C^2} = \frac{-2}{\epsilon \epsilon_0 q N_A} \left( E - E_{fb} - \frac{kT}{q} \right) \quad (7)$$

where  $\epsilon$  and  $\epsilon_0$  are the dielectric constant of the photocathode and the vacuum permittivity, respectively.  $q$ ,  $E_{fb}$ ,  $k$ , and  $N_A$  are the electron charge ( $1.6 \times 10^{-19}$  C), the flat-band potential, the Boltzmann constant ( $1.38 \times 10^{-23}$  J K<sup>-1</sup>), and the acceptor (hole) density (concentration), respectively. In p-type semiconductors, the linear slope of the Mott–Schottky plot should be negative, because the hole density is increased as the bias voltage becomes more negative.<sup>37</sup> The slope is positive for n-type semiconductors.<sup>38</sup>

Fig. 6a shows the Mott–Schottky curves for different Ni/CuO F samples. The capacitance ( $C^2$ ), which is the reciprocal of the y-axis in Fig. 6a, is gradually decreased from  $6.42 \times 10^{10}$  to  $1.12 \times 10^9$  F<sup>-2</sup> cm<sup>4</sup>. In other words, greater electrospinning durations for the Ni Fs correspond to higher acceptor concentrations. However,  $E_{fb}$  is increased from 0.246 to 0.308 V as  $t_e$  increases from 5 to 20 s, and decreases to 0.255 V for  $t_e = 30$  s. As shown in Fig. 6b, the acceptor concentration is increased from  $1.27 \times 10^{17}$  to  $1.46 \times 10^{17}$  for  $t_e$  of 5–20 s before decreasing to  $1.09 \times 10^{17}$  cm<sup>-3</sup> at  $t_e = 30$  s. The acceptor concentration is highest for  $t_e = 20$  s with a  $\sim 14\%$  increase compared to that

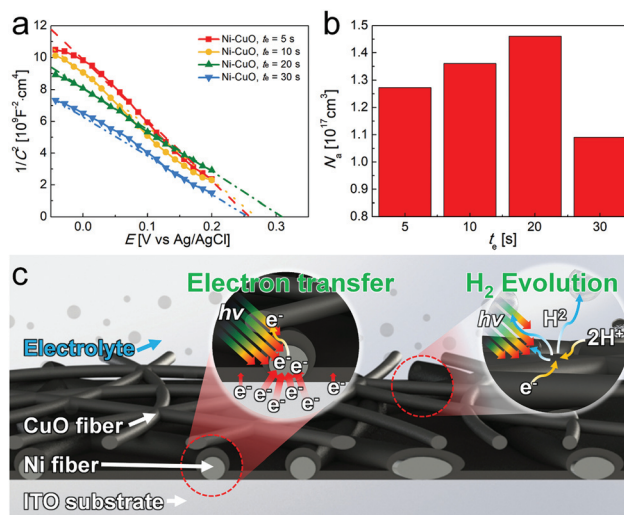


Fig. 6 (a) The Mott–Schottky curves obtained at 1000 Hz and (b) the hole concentration ( $N_A$ ) for  $t_e = 5, 10, 20$ , and  $30$  s. (c) Schematic of the mechanism of electron transfer and H<sub>2</sub> evolution on the Ni–CuO F photocathode.

for  $t_e = 5$  s. Therefore, the highest PCD shown in Fig. 4a corresponds to the enhanced acceptor concentration as well as improved charge separation.

Faradaic efficiency ( $\eta_F$ ) of water splitting is defined as the ratio of the current that produces H<sub>2</sub>/O<sub>2</sub> evolution to the total current that flows during photoelectrochemical reactions; it can also be expressed as the ratio of the volume of hydrogen produced to the theoretical volume that would be produced if all of the current produced hydrogen, as follows:<sup>39</sup>

$$\eta_F = \frac{V_{\text{exp}}}{V_{\text{theo}}} = \frac{V_{\text{exp}}}{(N_H \times Q \times V_m) / (N \times F)} \quad (8)$$

where  $V_{\text{exp}}$  and  $V_{\text{theo}}$  are the experimental and theoretical volumes of H<sub>2</sub> respectively.  $N_H$ ,  $Q$ , and  $V_m$  are the moles of H<sub>2</sub> per mole of H<sub>2</sub>O (for H<sub>2</sub>  $N_H = 2$ ), the total charge supplied to the electrode (current integrated over time), and the molar volume of H<sub>2</sub> ( $24.1 \text{ L mol}^{-1}$  at 293 K and 1 atm), respectively.  $N$  is the electrons per mole of H<sub>2</sub>O ( $N = 4$ ) and  $F$  is the Faraday constant ( $F = 96485 \text{ C mol}^{-1}$ ). For measuring  $\eta_F$  of  $t_e = 20$  s, a fixed potential of  $-0.5$  V was applied for 280 min. As shown in Fig. S3,†  $V_{\text{exp}}$  gradually increased to 1.65 ml as  $t$  from increased from 0 to 280. Over time,  $\eta_F$  remained constant at 76% after 280 min. The details of H<sub>2</sub> measurements are presented in ESI.†

Fig. 6c schematically illustrates the electron excitation, emphasizing the important role of conductive Ni Fs to provide rapid electron-transfer pathways. The Ni Fs, in addition to providing faster electron transport, contribute significantly to controlling the electron–hole separation of the adjoining over-layer (CuO) for the efficient evolution of H<sub>2</sub>. The magnified cross-section of the ITO, Ni F under-layer, and CuO shows the transfer of the majority of electrons from the ITO to the Ni Fs; only a few electrons are passed to the CuO layer. Thus, under illumination (see the right-side magnified picture in Fig. 6c),

H<sub>2</sub> evolves as H<sup>+</sup> consuming photoexcited electrons generated in CuO. Therefore, more Ni Fs at  $t_e = 20$  s case (see the SEM images in the second row in Fig. 2c) provides additional channels for free electrons to the CuO layer which yielded a superior PCD performance. However, with further increase in the Ni F electrospinning time ( $t_e = 30$  s), the fiber diameter decreases and number of fibers increases. In this case, the acceptor concentration decreased producing lower  $R_{ct2}$  and consequently poor photocurrent density. Because of larger number of electrons transferring from Ni Fs throughout the network and rapid recombination (*i.e.*, lower recombination time  $\tau_n \sim 0.79$  ms), the acceptor concentration was reduced for the  $t_e = 30$  s sample; see Fig. 6b. Therefore, the reverse phenomenon occurred between  $t_e = 20$  s and 30 s.

## 4. Conclusion

The use of Ni-core Cu-shell fibers as photocathode materials was demonstrated for the first time. The initial electrospun polymer fiber was seeded with Pt and then electroplated sequentially with Ni and Cu to form a continuous core-shell fiber. The annealing treatment converted the outer Cu shell to CuO for use as a photoactive semiconducting material, while the inner Ni core remained purely metallic with high electrical conductivity. This facilitated a high electron mobility, high carrier concentration, and long carrier lifetime, suppressing recombination in the photocathode. The Ni-core fiber showed overall improved PEC performance, with a 2.6-fold increase in PCD compared to the CuO fiber with no Ni core. The optimal amount of Ni was identified by varying the electrospinning time for Ni; the optimum electrospinning time was established as 20 s.

## Conflicts of interest

There are no conflicts to declare.

## Acknowledgements

This research was supported by the Technology Development Program to Solve Climate Changes of the National Research Foundation (NRF) funded by the Ministry of Science, ICT & Future Planning (NRF-2016M1A2A2936760) and NRF-2017R1A2B4005639.

## References

- 1 Y. Yang, D. Xu, Q. Wu and P. Diao, *Sci. Rep.*, 2016, **6**, 35158.
- 2 H. Qi, J. Wolfe, D. Fichou and Z. Chen, *Sci. Rep.*, 2016, **6**, 30882.
- 3 C. Jiang, S. J. Moniz, A. Wang, T. Zhang and J. Tang, *Chem. Soc. Rev.*, 2017, **46**, 4645–4660.
- 4 Y.-F. Lim, C. S. Chua, C. J. J. Lee and D. Chi, *Phys. Chem. Chem. Phys.*, 2014, **16**, 25928–25934.
- 5 Q. Huang, F. Kang, H. Liu, Q. Li and X. Xiao, *J. Mater. Chem. A*, 2013, **1**, 2418–2425.
- 6 Z. Zhang, R. Dua, L. Zhang, H. Zhu, H. Zhang and P. Wang, *ACS Nano*, 2013, **7**, 1709–1717.
- 7 J. Hou, C. Yang, H. Cheng, S. Jiao, O. Takeda and H. Zhu, *Energy Environ. Sci.*, 2014, **7**, 3758–3768.
- 8 D. Cao, N. Nasori, Z. Wang, Y. Mi, L. Wen, Y. Yang, S. Qu, Z. Wang and Y. Lei, *J. Mater. Chem. A*, 2016, **4**, 8995–9001.
- 9 S. N. F. M. Nasir, M. K. N. Yahya, N. W. M. Sopian, N. A. Ludin, M. A. Ibrahim, K. Sopian and M. A. M. Teridi, *RSC Adv.*, 2016, **6**, 56885–56891.
- 10 Q. Lu, J. Rosen and F. Jiao, *ChemCatChem*, 2015, **7**, 38–47.
- 11 M.-w. Kim, H. Yoon, T. Y. Ohm, H. S. Jo, S. An, S. K. Choi, H. Park, S. S. Al-Deyab, B. K. Min, M. T. Swihart and S. S. Yoon, *Appl. Catal., B*, 2017, **201**, 479–485.
- 12 C.-Y. Chiang, Y. Shin and S. Ehrman, *Appl. Energy*, 2016, **164**, 1039–1042.
- 13 J.-w. Ha, J. Oh, H. Choi, H. Ryu, W.-J. Lee and J.-S. Bae, *J. Ind. Eng. Chem.*, 2017, **58**, 38–44.
- 14 S. Baturay, A. Tombak, D. Kaya, Y. S. Ocak, M. Tokus, M. Aydemir and T. Kilicoglu, *J. Sol-Gel Sci. Technol.*, 2016, **78**, 422–429.
- 15 A. A. Dubale, C.-J. Pan, A. G. Tamirat, H.-M. Chen, W.-N. Su, C.-H. Chen, J. Rick, D. W. Ayele, B. A. Aragaw and J.-F. Lee, *J. Mater. Chem. A*, 2015, **3**, 12482–12499.
- 16 B. G. Streetman and S. K. Banerjee, *Solid state electronic devices*, Prentice-Hall, 2005.
- 17 F. A. Akgul, G. Akgul, N. Yildirim, H. E. Unalan and R. Turan, *Mater. Chem. Phys.*, 2014, **147**, 987–995.
- 18 M. Al-Kuhaili, *Vacuum*, 2008, **82**, 623–629.
- 19 M. Nair, L. Guerrero, O. L. Arenas and P. Nair, *Appl. Surf. Sci.*, 1999, **150**, 143–151.
- 20 M. R. Johan, M. S. M. Suan, N. L. Hawari and H. A. Ching, *Int. J. Electrochem. Sci.*, 2011, **6**, 6094–6104.
- 21 J. Zhang and X. Wang, *Angew. Chem., Int. Ed.*, 2015, **54**, 7230–7232.
- 22 L. Zhu, M. Hong and G. W. Ho, *Nano Energy*, 2015, **11**, 28–37.
- 23 K. Munawar, M. A. Mansoor, W. J. Basirun, M. Misran, N. M. Huang and M. Mazhar, *RSC Adv.*, 2017, **7**, 15885–15893.
- 24 B. Šljukić, C. E. Banks, A. Crossley and R. G. Compton, *Electroanalysis*, 2007, **19**, 79–84.
- 25 D. S. Kozak, R. A. Sergiienko, E. Shibata, A. Iizuka and T. Nakamura, *Sci. Rep.*, 2016, **6**, 21178.
- 26 D. Tahir and S. Tougaard, *J. Phys.: Condens. Matter*, 2012, **24**, 175002.
- 27 D. Svintsitskiy, A. Stadnichenko, D. Demidov, S. Koscheev and A. Boronin, *Appl. Surf. Sci.*, 2011, **257**, 8542–8549.
- 28 Z. Gan, G. Yu, B. K. Tay, C. Tan, Z. Zhao and Y. Q. Fu, *J. Phys. D: Appl. Phys.*, 2003, **37**, 81.
- 29 N. Ghobadi, *Int. Nano Lett.*, 2013, **3**, 2.
- 30 R. López and R. Gómez, *J. Sol-Gel Sci. Technol.*, 2012, **61**, 1–7.
- 31 C. Xia, L. Cao, W. Liu, G. Su, R. Gao, H. Qu, L. Shi and G. He, *CrystEngComm*, 2014, **16**, 7469–7477.
- 32 M. Choi, J. H. Lee, Y. J. Jang, D. Kim, J. S. Lee, H. M. Jang and K. Yong, *Sci. Rep.*, 2016, **6**, 36099.

- 33 Q. Wang, S. Ito, M. Grätzel, F. Fabregat-Santiago, I. Mora-Seró, J. Bisquert, T. Bessho and H. Imai, *J. Phys. Chem. B*, 2006, **110**, 25210–25221.
- 34 J. Bisquert, A. Zaban, M. Greenshtein and I. Mora-Seró, *J. Am. Chem. Soc.*, 2004, **126**, 13550–13559.
- 35 Y. J. Jang, J.-W. Jang, S. H. Choi, J. Y. Kim, J. H. Kim, D. H. Youn, W. Y. Kim, S. Han and J. S. Lee, *Nanoscale*, 2015, **7**, 7624–7631.
- 36 W. Gomes and D. Vanmaekelbergh, *Electrochim. Acta*, 1996, **41**, 967–973.
- 37 D. Xiong, Q. Zhang, Z. Du, S. K. Verma, H. Li and X. Zhao, *New J. Chem.*, 2016, **40**, 6498–6504.
- 38 L. Jinlong and L. Hongyun, *Surf. Coat. Technol.*, 2013, **235**, 513–520.
- 39 S. Zhao, J. Huang, Y. Liu, J. Shen, H. Wang, X. Yang, Y. Zhu and C. Li, *J. Mater. Chem. A*, 2017, **5**, 4207–4214.